

MID-INFRARED POLYCYCLIC AROMATIC HYDROCARBON AND H₂ EMISSION AS A PROBE OF PHYSICAL CONDITIONS IN EXTREME PHOTODISSOCIATION REGIONS

O. BERNÉ¹, A. FUENTE², J. R. GOICOECHEA¹, P. PILLERI^{3,4}, M. GONZÁLEZ-GARCÍA⁵, AND C. JOBLIN^{3,4}

¹ Centro de Astrobiología (CSIC/INTA), Laboratorio de Astrofísica Molecular, Ctra. de Torrejón a Ajalvir, km 4 28850, Torrejón de Ardoz, Madrid, Spain

² Observatorio Astronómico Nacional, Apdo. Correos 112, 28803 Alcalá de Henares, Madrid, Spain

³ Université de Toulouse, UPS, CESR, 9 ave colonel Roche, F-31028 Toulouse cedex 9, France

⁴ CNRS, UMR 5187, 31028 Toulouse, France

⁵ LUTH, Observatoire de Paris and Université Paris, 7 place Jansen, 92190 Meudon, France

Received 2009 July 21; accepted 2009 October 20; published 2009 November 4

ABSTRACT

Mid-infrared (mid-IR) observations of polycyclic aromatic hydrocarbons (PAHs) and molecular hydrogen emission are a potentially powerful tool to derive physical properties of dense environments irradiated by intense UV fields. We present new, spatially resolved, *Spitzer* mid-IR spectroscopy of the high UV field and dense photodissociation region (PDR) around Monoceros R2, the closest ultracompact H II region, revealing the spatial structure of ionized gas, PAHs, and H₂ emissions. Using a PDR model and PAH emission feature fitting algorithm, we build a comprehensive picture of the physical conditions prevailing in the region. We show that the combination of the measurement of PAH ionization fraction and of the ratio between the H₂ 0–0 *S*(3) and *S*(2) line intensities, respectively, at 9.7 and 12.3 μm, allows us to derive the fundamental parameters driving the PDR: temperature, density, and UV radiation field when they fall in the ranges $T = 250\text{--}1500$ K, $n_{\text{H}} = 10^4\text{--}10^6$ cm⁻³, and $G_0 = 10^3\text{--}10^5$, respectively. These mid-IR spectral tracers thus provide a tool to probe the similar but unresolved UV-illuminated surface of protoplanetary disks or the nuclei of starburst galaxies.

Key words: infrared: ISM – ISM: lines and bands – ISM: molecules

1. INTRODUCTION

Dense ($> 10^4$ cm⁻³) and high UV field ($> 10^4$ times the standard interstellar radiation field in units of the Habing field, written G_0 hereafter) photodissociation regions (PDRs) rule the energy balance, and thus evolution, of some of the most fundamental astrophysical objects such as protoplanetary disks, planetary nebulae, and starburst galaxies. One of the best tools to probe this UV-illuminated matter is spectroscopy in the mid-infrared (hereafter mid-IR; 5–15 μm) because it provides information on both the gas and small dust grain properties (polycyclic aromatic hydrocarbons and very small grains, hereafter PAHs and VSGs). Ideally, one would like to spatially resolve the emission of these components in order to study their variations as the UV field is attenuated. Unfortunately, such observations are very hard to achieve (for the moment), on one hand because large ground-based telescopes, providing arcsecond angular resolution, are restrained in wavelength coverage, while on the other hand, space-borne telescopes have diameters that are usually too small to resolve the sources. Because it is the closest ultracompact H II region at a distance of 850 pc, Monoceros R2 (Mon R2; see Wood & Churchwell 1989; Howard et al. 1994) constitutes one of the rare exceptions where one can resolve the PDR between the H II region and molecular cloud. In this Letter, we present and analyze the mid-IR PAH and molecular hydrogen emissions in Mon R2 based on spatially resolved *Spitzer* spectral mapping.

2. OBSERVATIONS

Mon R2 was observed using the Infrared Spectrograph (IRS) on board *Spitzer*, in the low-resolution mode ($\lambda/\Delta\lambda = 60\text{--}127$) as part of the “SPECHIP” program (PI: C. Joblin). The data were obtained in the spectral mapping mode. The full spectral cubes of the SL1 and SL2 modules were built using the CUBISM software (Smith et al. 2007) from the basic calibrated files

retrieved from the *Spitzer* archive (ver. S19 pipeline). The two cubes were then assembled to provide the full SL cube of 26×36 positions in space and ~ 170 points in wavelength, ranging from 5 to 14.5 μm.

3. OBSERVATIONAL RESULTS

An overview of our observations is presented in Figure 1. The ionized gas in the H II region, traced by the [Ne II] line at 12.8 μm, appears confined in a spherical region, as seen by radio continuum observations (Wood & Churchwell 1989) and in higher angular and spectral resolution [Ne II] ground-based observations (Takahashi et al. 2000; Jaffe et al. 2003). The cometary shape of the H II region is well seen in our [Ne II] map and peaks at about 0.12 erg s⁻¹ cm⁻² sr⁻¹ in the surroundings of the B1 star IRS1. The fact that [Ne II] maximum contours do not include the exact position of IRS1 is due to the saturation of the IRS detectors at this position, implying that the intensity could not be measured, though likely peaking there as shown by Takahashi et al. (2000) and Jaffe et al. (2003). PAH emission is present everywhere in the region, but for clarity in Figure 1 we only present the region where it is the brightest in the 11.3 μm band ($1\text{--}4 \times 10^{-2}$ erg s⁻¹ cm⁻² sr⁻¹), forming a filamentary/shell structure that surrounds the H II region. The H₂ 0–0 *S*(3) rotational line at 9.7 μm peaks in a filament that lies between the H II region and the cold and dense molecular gas traced by CS $J = 5\text{--}4$ (Figure 1) transition. The intensity of the H₂ 0–0 *S*(3) line is of the order of $(1\text{--}4) \times 10^{-4}$ erg s⁻¹ cm⁻² sr⁻¹. The H₂ 0–0 *S*(2) line at 12.3 μm follows a similar spatial distribution. As in the Orion bar (Tielens et al. 1993), the spatial distribution of these H₂ lines is not correlated with the PAH emission contrary to what is seen in lower UV field PDRs like the Horsehead nebula (Habart et al. 2003; Compiègne et al. 2007) or the ρ -Ophiucus filament (Habart et al. 2005). In the following, we investigate the origin of these structures from a physical point of view, using PAH emission and modeling the H₂ excitation in

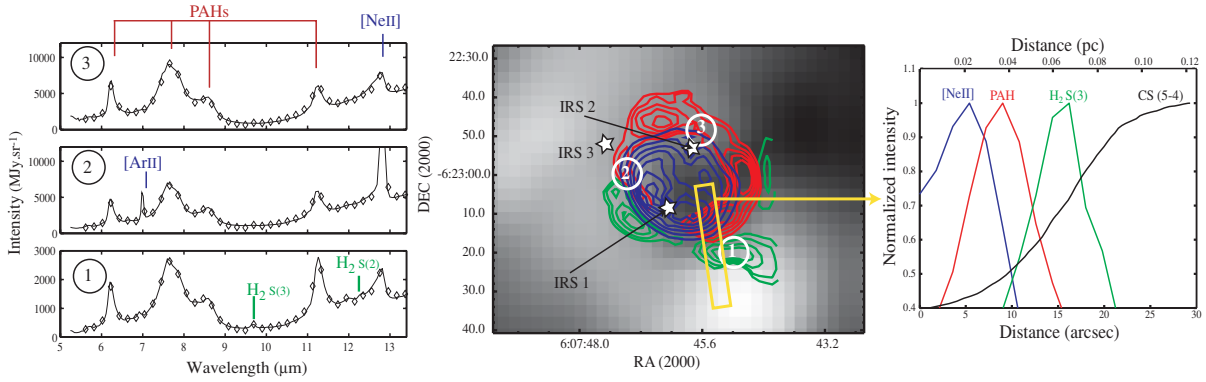


Figure 1. Overview of the Mon R2 region seen with *Spitzer*. Left: observed IRS spectra for PDRs 1, 2, and 3 (continuous line) and fit by the model (diamonds, see Section 4.2.1). Middle: the blue contours represent the intensity of the [Ne II] line ($0.02\text{--}0.1 \text{ erg s}^{-1} \text{ cm}^{-2} \text{ sr}^{-1}$ in linear steps), the red contours the intensity of the PAH $11.3 \mu\text{m}$ band ($1.8\text{--}3.4 \times 10^{-2} \text{ erg s}^{-1} \text{ cm}^{-2} \text{ sr}^{-1}$ in linear steps), and the green contours the intensity of the H₂ 0–0 emission in the S(3) rotational line at $9.7 \mu\text{m}$ ($1.5\text{--}4.5 \times 10^{-4} \text{ erg s}^{-1} \text{ cm}^{-2} \text{ sr}^{-1}$ in linear steps). The background map shows the CS $J = 5\text{--}4$ emission presented in Choi et al. (2000). Low emission is in black. Numbers indicate the positions of the selected PDRs. Right: cut in the map along the yellow box, showing the stratified emission of the different lines.

the PDR. To simplify the task, we select three different zones named PDR 1, PDR 2, and PDR 3 as displayed in Figure 1. PDR 1 was chosen to be representative of the region where the maximum of H₂ emission is found (PAH emission is weaker but present). PDR 2 is the transition from the H II region to the molecular gas. At these two positions, it is well seen that H₂ gas is found further from the star than the PAH emission (see cut in Figure 1). Finally, we positioned PDR 3 in a region situated further from IRS1, which is a smoother transition from ionized to neutral and molecular gas. For comparison, we also consider the mid-IR spectrum obtained by integrating the whole IRS cube over the area imaged.

4. PROBING THE PHYSICAL CONDITIONS OF A HIGH UV FIELD, HIGH-DENSITY PDR

4.1. H₂ Emission as a Probe of Gas Density and Temperature

In dense and high-UV PDRs like Mon R2, the excitation of the H₂ pure rotational lines is dominated by inelastic collisions (Le Boulrot et al. 1999). To quantitatively probe the role of density n_{H} and radiation field G_0 on the excitation of the lowest energy rotational levels of H₂, we use the revised Meudon PDR code (Le Petit et al. 2006; Goicoechea & Le Boulrot 2007) for a large grid of radiation fields and densities above 10^3 cm^{-3} . Since the critical density of the S(3) line is $\sim 5 \times 10^4 \text{ cm}^{-3}$ (Le Boulrot et al. 1999), the lowest energy rotational levels are thermalized when $n_{\text{H}} \gtrsim 5 \times 10^4 \text{ cm}^{-3}$. As a consequence, the S(3)/S(2) line ratio scales with the gas temperature and $T_{\text{rot}} \simeq T$, where T_{rot} is the rotational temperature of the associated rotational transition. In high-UV high-density PDRs, the main mechanism heating the gas is the photoelectric heating by electrons ejected from very small dust grains and PAHs. Thus, the photoelectric heating efficiency will depend on the ability to eject electrons from the grain surface (less efficient as grains become positively charged) and on the density of electrons in the gas with which charged grains recombine and neutralize. In PDRs, low-energy electrons are provided by the ionization of carbon atoms, and as essentially all the carbon is ionized, the electron density depends on gas density and carbon abundance. Overall, as the elemental abundance [C]/[H] is constant, an increase of the gas density (thus of electron density) reduces the grains charge and increases the photoelectric heating efficiency (i.e., the gas temperature). This explains the dependence of the S(3)/S(2) ratio with density seen in Figure 2.

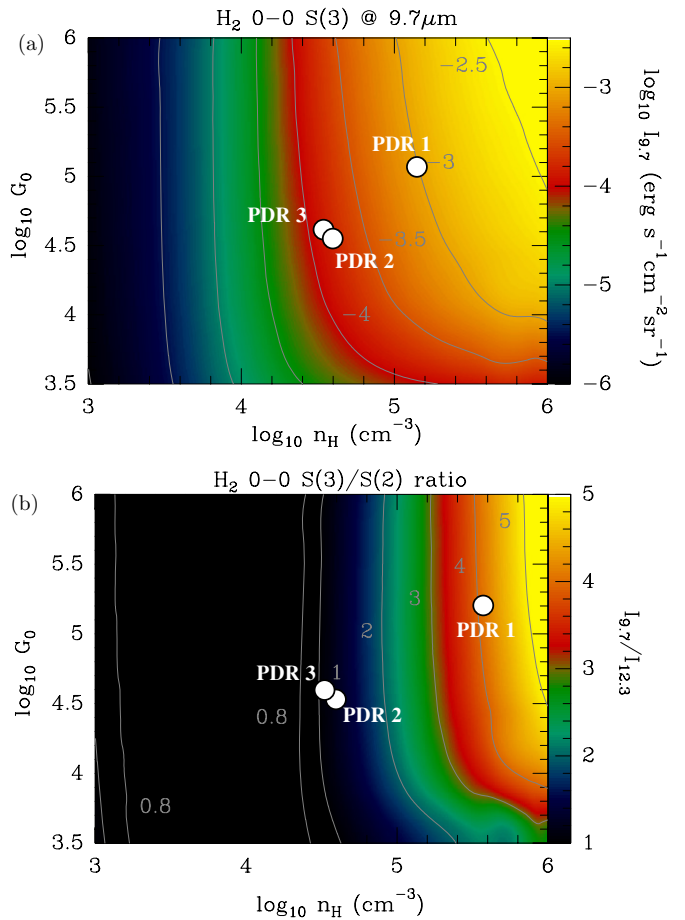


Figure 2. Results from the Meudon PDR code for high UV field/density conditions. (a) Variations of the H₂ 0–0 S(3) absolute intensity (colors and contours) as a function of the hydrogen nuclei density n_{H} and intensity of the radiation field G_0 . (b) Variations of the S(3)/S(2) line ratio (colors and contours) as a function of n_{H} and G_0 . Circles indicate the intersection between observed values of $I_{S(3)}$ (panel (a)) and $I_{S(3)}/I_{S(2)}$ (panel (b)) and the G_0 derived using PAH ionization fraction for PDRs 1, 2, and 3.

4.2. PAHs as a Probe of Radiation Field

4.2.1. Mid-IR Emission Model

In order to analyze the full *Spitzer* mid-IR cube, we use a model adapted from Joblin et al. (2008) and Berné et al. (2009). This emission model includes the four major dust components,

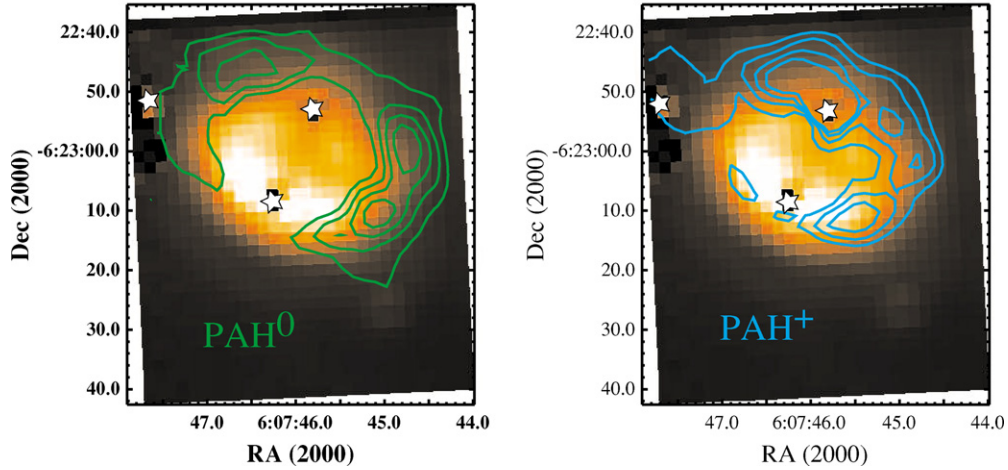


Figure 3. Contours of PAH⁰ and PAH⁺ intensity (resp. green and blue) overlaid on [Ne II] intensity map, built from the results of the fit obtained for each spectrum of the cube of Mon R2. Positions of IRS1, 2, and 3 marked as in Figure 1.

Table 1
Observational Diagnostics in PDR 1, PDR 2, and PDR 3

Position	H ₂ Lines (Corrected from Extinction)			Fit of PAH Bands			
	$I_{S(2)}$ (erg cm ⁻² s ⁻¹ sr ⁻¹)	$I_{S(3)}$ (erg cm ⁻² s ⁻¹ sr ⁻¹)	$I_{S(3)}/I_{S(2)}$ (K)	A_V	$I_{6.2}/I_{11.3}$	$\frac{[\text{PAH}^+]}{[\text{PAH}^0]}$	$\frac{G_0\sqrt{T}/10^3}{n_H}$ (K ^{1/2} cm ⁻³)
PDR 1	$2.3^{\pm 0.15} \times 10^{-4}$	$9.6^{\pm 0.1} \times 10^{-4}$	$4.2^{\pm 0.30}$	16	1.1	0.03	0.28
PDR 2	$1.6^{\pm 0.1} \times 10^{-4}$	$2.1^{\pm 0.1} \times 10^{-4}$	$1.3^{\pm 0.15}$	12	1.8	1.60	0.49
PDR 3	$1.8^{\pm 0.1} \times 10^{-4}$	$2.0^{\pm 0.1} \times 10^{-4}$	$1.1^{\pm 0.15}$	19	2.0	2.44	0.56
Mon R2 ^a	$8.0^{\pm 0.1} \times 10^{-5}$	$10.3^{\pm 0.1} \times 10^{-5}$	$1.3^{\pm 0.10}$	9	1.9	1.9	0.52

Notes. Observational errors are given for H₂ lines.

^a Spectrum obtained integrating the IRS cube over area imaged.

introduced in these previous works: VSGs (small carbonaceous dust grains), free neutral PAHs, positively ionized PAHs (PAH⁺), and finally PAH^x that are large (with $N_C > 100$ carbon atoms) charged PAHs. We decompose the observed mid-IR emission using the four template spectra presented in Berné et al. (2009). In addition, we consider continuum emission that is simply modeled with two slopes. Furthermore, we include the effect of extinction by multiplying the mid-IR spectrum by $(1 - e^{-\tau_\lambda})/\tau_\lambda$, where $\tau_\lambda = C_{\text{ext}}(\lambda) \cdot N_l$, $C_{\text{ext}}(\lambda)$ being the extinction cross section per nucleon, taken from Weigartner & Draine (2001) with $R_V = 5.5$ and N_l , the column density on material on the line of sight, is left as a free parameter in the fit. The values A_V of visual extinction corresponding to the derived N_l (related by $N_l = 1.8 \times 10^{21} A_V$) for each PDR, and used to correct the measured H₂ lines intensities as a function of their wavelength, are given in Table 1. We fit all the spectra of the cube using this technique, thus providing the spatial distributions of the emission of each component. An example of these fits is provided in Figure 1, and spatial distributions of PAH⁺ and PAH⁰ populations are presented in Figure 3.

4.2.2. Estimating G_0 Using PAH Ionization Ratio

As shown by models (Tielens 2005) and observations (e.g., Bregman & Temi 2005; Flagey et al. 2006; Galliano et al. 2008), the PAH ionization ratio ($[\text{PAH}^+]/[\text{PAH}^0]$) depends on the parameter $G_0\sqrt{T}/n_e$, where T is the gas temperature and n_e is the electron density. Ionization of PAHs will influence the emission cross section of these molecules so that the ratio between the 6.2 and 11.3 μm bands ($I_{6.2}/I_{11.3}$) will increase

with increasing $G_0\sqrt{T}/n_e$. Assuming that most electrons are provided by the ionization of carbon, we can write that $n_e \simeq x(\text{C}^+)n_H \simeq [\text{C}]/[\text{H}]n_H$, with $[\text{C}]/[\text{H}]$ the elemental abundance of carbon assumed to be 1.6×10^{-4} (Sofia et al. 2004). Finally, using the empirical law of Galliano et al. (2008), we can relate the $I_{6.2}/I_{11.3}$ to $G_0(T/10^3)^{1/2}/n_H$ by

$$G_0(T/10^3)^{1/2}/n_H \simeq (1990[\text{C}]/[\text{H}]) \times ((I_{6.2}/I_{11.3}) - 0.26). \quad (1)$$

Using the ratio between the 6.2 and 11.3 μm bands for neutral and ionized PAHs found in Table 1 in Rapacioli et al. (2005), we relate $I_{6.2}/I_{11.3}$ to the ionized to neutral PAH density ratio $\frac{[\text{PAH}^+]}{[\text{PAH}^0]}$, using Equation (2) in Joblin et al. (1996):

$$I_{6.2}/I_{11.3} = 1.12 \times \frac{1 + \frac{[\text{PAH}^+]}{[\text{PAH}^0]} \times 0.85}{1 + \frac{[\text{PAH}^+]}{[\text{PAH}^0]} \times 0.29}. \quad (2)$$

5. APPLICATION TO MON R2 PDRs

The high value of $I_{S(3)}$ we observe requires both $G_0 > 1 \times 10^4$ and $n_H > 1 \times 10^4 \text{ cm}^{-3}$ (Figure 2 and Burton et al. 1992; Kaufman et al. 2006). This implies that the observed $I_{S(3)}/I_{S(2)}$ ratio, after correction for extinction (Table 1), allows the derivation of the approximate densities of PDRs 1, 2, and 3 in Figure 2(b). In addition, since these lines are thermalized, the gas temperature, T , is coincident with the rotational temperature, T_{rot} , and we can infer T for the different PDRs (Table 2). To calculate the rotational temperature, we have assumed an ortho-para ratio of 3, that is the equilibrium value for temperatures

Table 2
Derived Physical Parameters for PDR 1, PDR 2, and PDR 3

Position	n_{H} (cm ⁻³)	T_{rot} (K)	G_0
PDR 1	$4.3^{±0.5} \times 10^5$	574^{+25}_{-22}	$1.6^{±0.2} \times 10^5$
PDR 2	$4.0^{±0.4} \times 10^4$	331^{+19}_{-17}	$3.3^{±0.3} \times 10^4$
PDR 3	$3.7^{±0.3} \times 10^4$	314^{+18}_{-16}	$3.7^{±0.2} \times 10^4$
Mon R2	$4.0^{±0.4} \times 10^4$	321^{+18}_{-16}	$3.7^{±0.4} \times 10^4$

Note. Errors are the result of propagation from those in Table 2.

larger than 100 K. Finally, using the value of $G_0(T/10^3)^{1/2}/n_{\text{H}}$ estimated with the PAH ionization fraction (or $I_{6.2}/I_{11.3}$), and the above derived T and $n_{\text{H}}H$, we can derive the intensity of the radiation field that illuminates the three PDRs and precisely position PDRs 1, 2, and 3 in Figure 2. The found values for n_{H} , T , and G_0 , (Table 2) are consistent with Mon R2 being a dense and highly UV irradiated PDR as estimated from other molecular lines (Choi et al. 2000; Rizzo et al. 2003, 2005). The found values for density are lower than in these previous works because the present tracers (PAHs and H₂) probe the outermost cloud regions directly exposed to the UV radiation field that are usually warmer (>500 K) and less dense than regions situated deeper into the molecular cloud (see cut in Figure 1). Finally, the estimated parameters using this technique, for the *entire* Mon R2 region (see Table 2), are more consistent with the ones derived for spatially resolved PDRs 2 and 3.

6. CONCLUSIONS

The main results we have presented in this Letter are (1) Mon R2 is a unique template of high-UV/high-density PDRs that is spatially resolved, similar to the Orion bar (where the UV field is slightly lower); (2) our observations are consistent with PDR models that predict that in high UV and dense PDRs, the excitation of pure rotational H₂ lines is collisional and depends on gas temperature; (3) for this reason, the spatial distributions of PAHs and warm H₂ are different, contrary to what is seen in cool PDRs; (4) however, because PAH emission is present in the extended region illuminated by the radiation, their ionization fraction can be used to probe the intensity of the UV radiation field, even where H₂ emission peaks. Thus, the mid-IR spectrum of dense and highly irradiated PDRs appears as an efficient probe of the physical conditions in these environments. The ratio between the molecular H₂ 0–0 $S(3)/S(2)$ line intensities allows to directly compute the density and temperature of the gas, while the measurement of the ionization fraction of PAHs allows to derive the intensity of the radiation field. We show that the derived parameters for the entire Mon R2 region are consistent with those found for the spatially resolved PDRs 2 and 3. This is likely because the dense PDR 1 occupies only a small part of the whole region, and therefore dilution effects imply that the spatially averaged spectrum is dominated by emission from lower density PDRs. Thus, we suggest that this spectral methodology could be useful to derive the dominant physical conditions in PDRs that are not spatially resolved in the mid-IR. In particular, the PDRs at the surface of protoplanetary disks around Herbig Ae/Be stars (Berné et al. 2009) or in the

inner rim of T Tauri disks (Agúndez et al. 2008) are expected to be the targets where such an analysis can be applied. The mid-IR spectrum of starburst galaxies is probably dominated by the emission of PDRs having similar conditions as those described in this Letter (see Fuente et al. 2008 for the case of M82). Thus, the present methodology could be a useful tool to derive global properties of galaxies, in connection with massive star formation activity, using the forthcoming *James Webb Space Telescope* and SPICA telescope, which will observe these emission features at low and high redshifts.

We thank the anonymous referee for constructive criticism and a careful reading of the manuscript. This work is based on observations made with the *Spitzer Space Telescope*, which is operated by the Jet Propulsion Laboratory, California Institute of Technology under NASA contract 1407. O.B. is supported by JAE-Doc CSIC fellowship. J.R.G. was supported by a Ramon y Cajal research contract from the spanish MICINN and co-financed by the European Social Fund. O.B., P.P., and C.J. acknowledge the french national program PCMI.

REFERENCES

- Agúndez, M., Cernicharo, J., & Goicoechea, J. R. 2008, *A&A*, 483, 831
 Berné, O., Joblin, C., Fuente, A., & Ménard, F. 2009, *A&A*, 495, 827
 Bregman, J., & Temi, P. 2005, *ApJ*, 621, 831
 Burton, M. G., Hollenbach, D. J., & Tielens, A. G. G. 1992, *ApJ*, 399, 563
 Choi, M., Evans, N. J., Tafalla, M., & Bachiller, R. 2000, *ApJ*, 538, 738
 Compiègne, M., Abergel, A., Verstraete, L., Reach, W. T., Habart, E., Smith, J. D., Boulanger, F., & Joblin, C. 2007, *A&A*, 471, 205
 Flagey, N., Boulanger, F., Verstraete, L., Miville Deschênes, M. A., Noriega Crespo, A., & Reach, W. T. 2006, *A&A*, 453, 969
 Fuente, A., et al. 2008, *A&A*, 492, 675
 Galliano, F., Madden, S. C., Tielens, A. G. G. M., Peeters, E., & Jones, A. P. 2008, *ApJ*, 679, 310
 Goicoechea, J. R., & Le Bourlot, J. 2007, *A&A*, 467, 1
 Habart, E., Abergel, A., Walmsley, C. M., Teyssier, D., & Pety, J. 2005, *A&A*, 437, 177
 Habart, E., Boulanger, F., Verstraete, L., Pineau des Forêts, G., Falgarone, E., & Abergel, A. 2003, *A&A*, 397, 623
 Howard, E. M., Pipher, J. L., & Forrest, W. J. 1994, *ApJ*, 425, 707
 Jaffe, D. T., Zhu, Q., Lacy, J. H., & Richter, M. 2003, *ApJ*, 596, 1053
 Joblin, C., Szczerba, R., Berné, O., & Szyszka, C. 2008, *A&A*, 490, 189
 Joblin, C., Tielens, A. G. G. M., Geballe, T. R., & Wooden, D. H. 1996, *ApJ*, 460, L119
 Kaufman, M. J., Wolfire, M. G., & Hollenbach, D. J. 2006, *ApJ*, 644, 283
 Le Bourlot, J., Pineau des Forêts, G., & Flower, D. R. 1999, *MNRAS*, 305, 802
 Le Petit, F., Nehmé, C., Le Bourlot, J., & Roueff, E. 2006, *ApJS*, 164, 506
 Rapacioli, M., Joblin, C., & Boissel, P. 2005, *A&A*, 429, 193
 Rizzo, J. R., Fuente, A., & García-Burillo, S. 2005, *ApJ*, 634, 1133
 Rizzo, J. R., Fuente, A., Rodríguez-Franco, A., & García-Burillo, S. 2003, *ApJ*, 597, L153
 Smith, J. D. T., et al. 2007, *PASP*, 119, 11335
 Sofia, U. J., Lauroesch, J. T., Meyer, D. M., & Cartledge, S. I. B. 2004, *ApJ*, 605, 272
 Takahashi, H., Matsuhara, H., Watarai, H., & Matsumoto, T. 2000, *ApJ*, 541, 779
 Tielens, A. G. G. M. 2005, *The Physics and Chemistry of the Interstellar Medium* (Cambridge: Cambridge Univ. Press)
 Tielens, A. G. G. M., Meixner, M. M., van der Werf, P., Bregman, J., Tauber, J. A., Stutzki, J., & Rank, D. 1993, *Science*, 262, 86
 Weingartner, J. C., & Draine, B. T. 2001, *ApJ*, 548, 296
 Wood, D. O. S., & Churchwell, E. 1989, *ApJS*, 69, 831